The Astrophysical Journal, 997:72 (10pp), 2026 January 20 https://doi.org/10.3847/1538-4357/ae285c

SN 2025coe: A Multiple-peaked Calcium-strong Transient from a White-dwarf Progenitor

Chun Chen[1,2,3], Ning-Chen Sun[4,5,6], Qiang Xi[4,5], Samaporn Tinyanont[7], David Aguado[8,9], Ismael Pérez-Fournon[8,9], Frédérick Poidevin[8,9], Justyn R. Maund[10], Amit Kumar[10], Junjie Jin[5], Yiming Mao[4,5], Beichuan Wang[4,5], Yu Zhang[5], Zhen Guo[11,12], Wenxiong Li[5], César Rojas-Bravo[4,5], Rong-Feng Shen[1,2], Lingzhi Wang[13,14], Ziyang Wang[4,5], Guoying Zhao[1,2], Jie Zheng[5], Yinan Zhu[5], David López Fernández-Nespral[8,9], Alicia López-Oramas[8,9], Zexi Niu[4,5], Yanan Wang[5], Klaas Wiersema[15], and Jifeng Liu[4,5,6]

[1] School of Physics and Astronomy, Sun Yat-sen University, Zhuhai 519082, People's Republic of China
[2] CSST Science Center for the Guangdong-Hong Kong-Macau Greater Bay Area, Sun Yat-sen University, Zhuhai 519082, People's Republic of China
[3] Dipartimento di Fisica, Università di Napoli "Federico II," Compl. Univ. di Monte S. Angelo, Via Cinthia, I-80126, Napoli, Italy
[4] School of Astronomy and Space Science, University of Chinese Academy of Sciences, Beijing 100049, People's Republic of China; sunnc@ucas.ac.cn
[5] National Astronomical Observatories, Chinese Academy of Sciences, Beijing 100101, People's Republic of China
[6] Institute for Frontiers in Astronomy and Astrophysics, Beijing Normal University, Beijing, 102206, People's Republic of China
[7] National Astronomical Research Institute of Thailand, 260 Moo 4, Donkaew, Maerim, Chiang Mai, 50180, Thailand
[8] Instituto de Astrofísica de Canarias, Vía Láctea, 38205, La Laguna, Tenerife, Spain
[9] Universidad de La Laguna, Departamento de Astrofísica, 38206, La Laguna, Tenerife, Spain
[10] Department of Physics, Royal Holloway, University of London, Egham, TW20 0EX, UK
[11] Instituto de Física y Astronomía, Universidad de Valparaíso, ave. Gran Bretaña, 1111, Casilla 5030, Valparaíso, Chile
[12] Millennium Institute of Astrophysics, Nuncio Monseñor Sotero Sanz 100, Of. 104, Providencia, Santiago, Chile
[13] Chinese Academy of Sciences South America Center for Astronomy (CASSACA), National Astronomical Observatories, CAS, Beijing 100101, People's Republic of China
[14] Departamento de Astronomía, Universidad de Chile, Las Condes, 7591245 Santiago, Chile
[15] Centre for Astrophysics Research, University of Hertfordshire, Hatfield, AL10 9AB, UK
Received 2025 September 30; revised 2025 November 28; accepted 2025 December 1; published 2026 January 14

Abstract

SN 2025coe is a calcium-strong transient located at an extremely large projected offset ∼39.3 kpc from the center of its host, the nearby early-type galaxy NGC 3277 at a distance of ∼25.5 Mpc. In this paper, we present multiband photometric and spectroscopic observations spanning ∼100 days postdiscovery. Its multiband light curves display multiple distinct peaks: (1) an initial peak at $t \approx 1.6$ day attributed to shock cooling emission, (2) a secondary peak of $M_{R,\,\mathrm{peak}} \approx -15.8$ mag at $t \approx 10.2$ days powered by radioactive decay, and (3) a possible late-time bump at $t \approx 42.8$ days likely caused by ejecta–circumstellar material/clump interaction. Spectral evolution of SN 2025coe reveals a fast transition to the nebular phase within 2 months, where it exhibits an exceptionally high [Ca II]/[O I] ratio larger than 6. Modeling of the bolometric light curve suggests an ejecta mass of $M_{\mathrm{ej}} = 0.29^{+0.14}_{-0.15}\,M_{\odot}$, a ^{56}Ni mass of $M_{^{56}\mathrm{Ni}} = 2.4^{+0.06}_{-0.05} \times 10^{-2} M_{\odot}$, and a progenitor envelope with mass $M_e = 1.4^{+6.9}_{-1.2} \times 10^{-3}\,M_{\odot}$ and radius $R_e = 13.5^{+64.1}_{-11.1}\,R_{\odot}$. The tidal disruption of a hybrid HeCO white dwarf (WD) by a low-mass CO WD provides a natural explanation for the low ejecta mass, the small fraction of ^{56}Ni, and the presence of an extended, low-mass envelope.

Unified Astronomy Thesaurus concepts: Supernovae (1668)

Materials only available in the online version of record: data behind figures, machine-readable table

1. Introduction

Over the past two decades, the advent of time-domain astronomy has led to the discovery of an increasing number of transients. Among these, calcium-strong transients (CaSTs) represent a distinct class of supernovae (SNe) with low luminosity ($-14 < M_{R,\,\mathrm{peak}} < -16.5$), rapid evolution (post-peak decline rate ∼0.2 mag day^{-1} in the R band), unusually fast transition from photospheric to nebular phases (∼a few tens of days), and diverse light-curve morphologies with single-, double-, or even multiple-peaked profiles (K. De et al. 2018; W. V. Jacobson-Galán et al. 2020, 2022; K. Ertini et al. 2023). CaSTs are also known as Ca-rich SNe or Ca-rich gap transients (H. B. Perets et al. 2010; M. M. Kasliwal et al. 2012; A. W. Alsabti & P. Murdin 2017; R. Lunnan et al. 2017).

A defining feature of CaSTs is their exceptionally high nebular-phase [Ca II]/[O I] flux ratios (>2), first identified by A. V. Filippenko et al. (2003), H. B. Perets et al. (2010), and subsequently confirmed by extensive studies (M. M. Kasliwal et al. 2012; A. W. Alsabti & P. Murdin 2017; R. Lunnan et al. 2017; K. De et al. 2020). J. S. Mulchaey et al. (2014) argue that this class of transients contributes a very significant fraction of Calcium in the intracluster medium. However, recent work has demonstrated that the strong [Ca II] emission lines do not necessarily require anomalously high calcium abundances in the ejecta. A. Polin et al. (2021) show that even modest calcium mass fractions (∼1%) can produce the observed line strengths, which explains the growing preference for the name "CaSTs," instead of Ca-rich transients, as it reflects their spectroscopic rather than nucleosynthetic distinction (K. J. Shen et al. 2019).

Notably, nearly half of all CaSTs occur in early-type galaxies (E or S0 galaxies; A. W. Alsabti & P. Murdin 2017; P. Scherbak et al. 2025), with a significant fraction exhibiting large projected offsets (>20 kpc) from their host galactic centers (A. W. Alsabti & P. Murdin 2017). The remote locations of CaSTs can potentially be explained through two channels. One scenario suggests in situ formation of progenitor systems within the galactic halo (F. Yuan et al. 2013), though deep imaging surveys have ruled out associations with globular clusters or massive star populations at these explosion sites (J. D. Lyman et al. 2014). Alternatively, these systems may have been dynamically ejected from their host galaxies' central regions through gravitational interactions with supermassive BHs or SN kicks (J. D. Lyman et al. 2014; R. J. Foley 2015), requiring approximately 100 Myr to reach their current positions at typical ejection velocities of several hundred km s^{-1}.

However, a nonnegligible fraction of CaSTs also exhibit small projected offsets (<5 kpc) from their host galactic centers. Several events, such as iPTF 16hgs (K. De et al. 2018) and SN 2019ehk (W. V. Jacobson-Galán et al. 2020), have even been found to coincide with star-forming regions of their host galaxies. Note that there is still controversy regarding the classification of SN 2019ehk as a CaST, given that it is spectroscopically more similar to a Type IIb SN (K. De et al. 2021). Nevertheless, it remains unclear whether the three-dimensional physical distances of these events indeed exceed 5 kpc, as current observational evidence remains inadequate to support robust physical interpretations.

The progenitor systems of CaSTs remain unknown. The population of CaSTs with large projected offsets in early-type galaxies indicates that these events likely originate from white dwarf (WD)–related progenitors. Proposed mechanisms include (1) the tidal disruption of a WD by a neutron star or an intermediate-mass black hole (P. H. Sell et al. 2015), (2) the explosion of a sufficiently low-mass WD (S. A. Sim et al. 2012), (3) the accretion-induced collapse of a WD (S. Darbha et al. 2010), (4) the well-studied ".Ia model" involving helium shell detonation on the WD surface where the shock propagation fails to ignite the core (L. Bildsten et al. 2007; K. J. Shen et al. 2010; R. Waldman et al. 2011; S. E. Woosley & D. Kasen 2011; S. A. Sim et al. 2012; A. W. Alsabti & P. Murdin 2017), and (5) the double-WD merger model (A. Bobrick et al. 2017; H. B. Perets et al. 2019; Y. Zenati et al. 2019). Another group of CaSTs located near galactic centers or within star-forming regions is considered to result from massive stellar explosions with completely stripped envelopes (K. De et al. 2021; T. Nakaoka et al. 2021). Therefore, resolving the origin of CaSTs remains an outstanding problem in time-domain astronomy.

SN 2025coe is a newly discovered CaST in the nearby universe, distinguished by its multipeaked light curve. It was first discovered by K. Itagaki (2025) on 2025 February 24 (MJD 60730.63) with a magnitude of 17.4 in the clear band at J2000 coordinates $\alpha = 10^{h}33^{m}07^{s}.95$, $\delta = +28^{\circ}\,26'\,13''.10$ (see Figure 1). The last nondetection before discovery was recorded on MJD 60729.5, i.e., ∼1 day before discovery, in the ATLAS *o* band. The host galaxy of SN 2025coe is NGC 3277, classified as an SAa/SAb-type galaxy with a redshift of $z = 0.00472$, corresponding to a luminosity distance of $D_L \approx 25.5$ Mpc (J. R. Mould et al. 2000). SN 2025coe is located at a projected distance of ∼317.″7 (∼39.3 kpc) from the nucleus of its host.

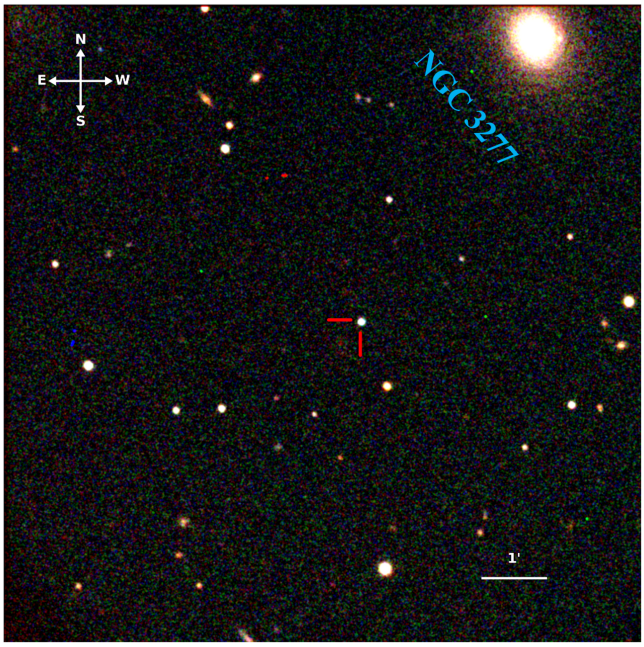

Figure 1. SN 2025coe and its host galaxy NGC 3277. The image is a composite of BV *R*-band observations obtained by TRT at $t = 1.7$ day after the discovery. The red cross marks the location of SN 2025coe.

We initiated multiband photometric and spectroscopic monitoring of SN 2025coe beginning approximately 1.5 day after its discovery. The combination of its close distance, early discovery with rapid follow-up observations, and remarkable features including a multipeaked light curve and substantial offset from the host galactic center provides an exceptional opportunity to advance our understanding of both the explosion mechanisms and progenitor systems of CaSTs. In this paper, we present detailed results of our study.

Throughout the paper, all epochs are relative to discovery (MJD = 60730.63) unless otherwise specified. Given that SN 2025coe is located far from its host galaxy, we only applied Galactic extinction corrections to the photometry; following dust maps in E. F. Schlafly & D. P. Finkbeiner (2011), we adopt $E(B-V) = 0.024$ and use the standard reddening law with $R_V = 3.1$ for the Galactic extinction correction (E. L. Fitzpatrick 1999).

The paper is organized as follows. In Section 2, we describe our long-term multiband photometric and spectroscopic monitoring. We provide a detailed analysis of these multiwavelength observations in Section 3. In Section 4, we construct the bolometric light curve of SN 2025coe and perform model fitting. In Section 5, we discuss our investigation into the progenitor system of SN 2025coe, with conclusions summarized in Section 6.

2. Observations

2.1. Photometry

We triggered target-of-opportunity follow-up observations of SN 2025coe with the Ultraviolet Optical Telescope (UVOT; P. W. A. Roming et al. 2005) on board the Neil Gehrels Swift Observatory (N. Gehrels et al. 2004) starting from 2025 February 26 until 2025 March 6 UTC ($t = 1.9$–10.3 days since discovery), with a cadence of 2 days using a sequence of filters

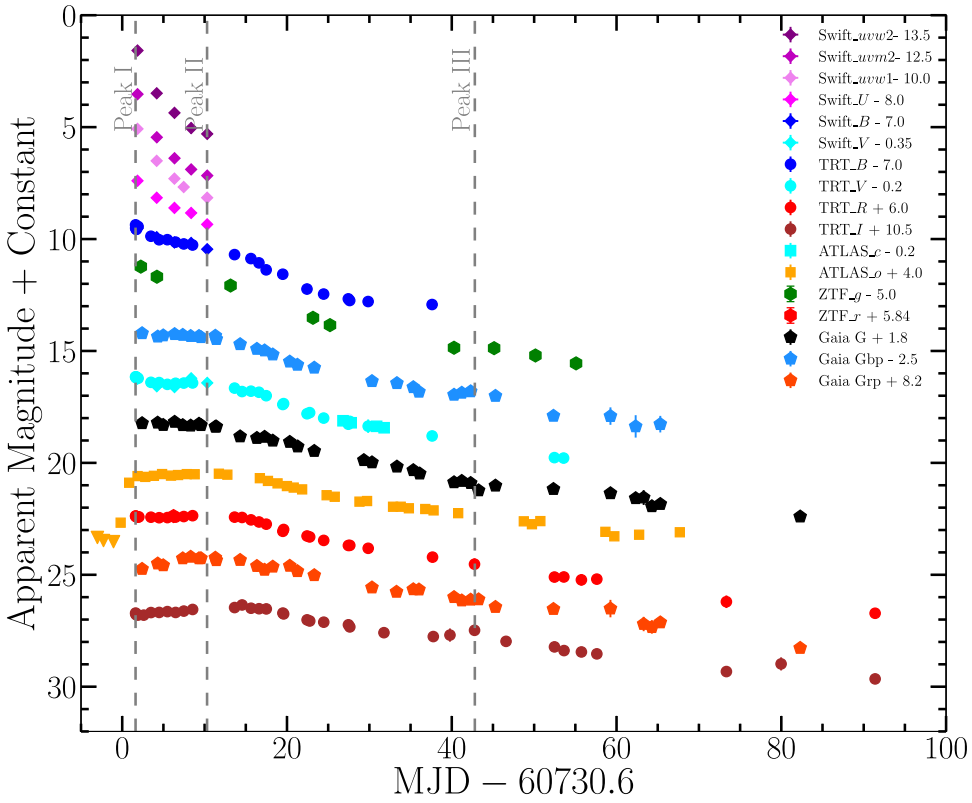

Figure 2. The multiband light curves of SN 2025coe are shown with phases relative to the first clear-band detection (MJD 60730.6). Gray dashed lines mark the epochs corresponding to the multiple photometric peaks. No extinction corrections are applied.

including *uvw*2, *uvm*2, *uvw*1, *U*, *B*, and *V*. We conducted aperture photometry using a 3″ aperture region with the `uvotsource` tool in `HEAsoft` v6.35 (along with the corresponding calibration files), following the standard procedures outlined in P. J. Brown et al. (2014). Given the isolation of SN 2025coe, no background subtraction is required. Results of photometry are listed in Table 1 and Figure 2. All magnitudes for Swift/UVOT are given in the Vega photometric system.

Besides, soon after the discovery of SN 2025coe, we rapidly triggered the Thai Robotic Telescope (TRT), obtaining the first data point at $t = 1.6$ day using a set of *BVRI* filters. The observations were conducted from its sites at the Sierra Remote Observatories, the Cerro Tololo Inter-American Observatory, and the Gao Mei Gu Observatory. Over the first 30 days, we use a typical cadence of 1–2 days. A lower cadence is adopted after $t \approx 30$ days, and we continue the follow-up observations out to $t = 91.4$ days after which SN 2025coe falls below the detection limit. Standard data reduction was applied, including bias subtraction and flat-field correction. Point-spread-function photometry was performed using `AutoPHOT` (S. J. Brennan & M. Fraser 2022). Photometric calibration was performed with the APASS catalog (A. A. Henden et al. 2009), converted into the Johnson–Cousins system using the method in R. Lupton & Ž. Ivezić (2005).

The RAPAS ProAm network (W. Thuillot et al. 2022) also conducted intensive monitoring of SN 2025coe from 2025 February 28 to May 29. They acquired 59 high-quality photometric measurements in their specialized filter system (RAPAS A/B/C bands precisely matched to Gaia DR3's G/Gbp/Grp passbands). These data are released to the public, and we retrieved their data from the Transient Name Server.[16]

In addition, we also retrieved the ATLAS (J. L. Tonry et al. 2018a, 2018b) and Zwicky Transient Facility (E. C. Bellm et al. 2019; M. J. Graham et al. 2019) data for SN 2025coe via the forced-photometry services.[17,18] These data points are also included in Table 1.

Table 1
UV-optical Photometry Results of SN 2025coe

MJD	Phase[a]	Filter	Magnitude	Uncertainty	Instrument
60730.4	–0.2	*o*	18.67	0.05	ATLAS
60731.4	+1.0	*o*	16.89	0.01	ATLAS
60732.2	+1.6	*B*	16.37	0.12	TRT
60732.2	+1.6	*V*	16.35	0.06	TRT
60732.2	+1.6	*R*	16.38	0.07	TRT
60732.2	+1.6	*I*	16.21	0.10	TRT
60732.3	+1.7	*B*	16.56	0.04	TRT
60732.3	+1.7	*V*	16.40	0.26	TRT
60732.3	+1.7	*R*	16.41	0.07	TRT
60732.3	+1.7	*I*	16.29	0.13	TRT

Notes. Here we only show the first 10 rows.
[a] Relative to discovery (MJD 60730.6).

(This table is available in its entirety in machine-readable form in the online article.)

[16] https://www.wis-tns.org/object/2025coe
[17] https://fallingstar-data.com/forcedphot/
[18] https://ztfweb.ipac.caltech.edu/cgi-bin/requestForcedPhotometry.cgi

Table 2
Optical Spectroscopy of SN 2025coe

MJD	Phase (days)	Filter	Grism	Spectral Range (Å)	Telescope/Instrument
60731.5	0.9	...	...	3200–5700, 5400–10000	LCO/FLOYDS-N
60732.1	1.5	...	...	4020–8100	LT/SPART
60732.8	2.2	385LP	G4	3700–8800	XL-216/BFOSC
60733.0	2.4	...	...	4020–8100	LT/SPART
60737.5	6.9	...	...	3200–5700, 5400–10000	LCO/FLOYDS-N
60738.8	8.2	385LP	G4	3700–8800	XL-216/BFOSC
60740.5	9.9	385LP	G4	3700–8800	XL-216/BFOSC
60742.5	11.9	385LP	G4	3700–8800	XL-216/BFOSC
60751.2	20.6	...	...	3200–5700, 5400–10000	LCO/FLOYDS-N
60752.0	21.4	...	...	4020–8100	LT/SPART
60768.0	37.4	...	...	4020–8100	LT/SPART
60783.9	53.3	...	...	4020–8100	LT/SPART
60790.9	60.3	...	...	4020–8100	LT/SPART
60818.0	87.4	...	R1000R	5100–10000	GTC/OSIRIS+

Note. The phase is indicated in the discovery SN 2025coe.

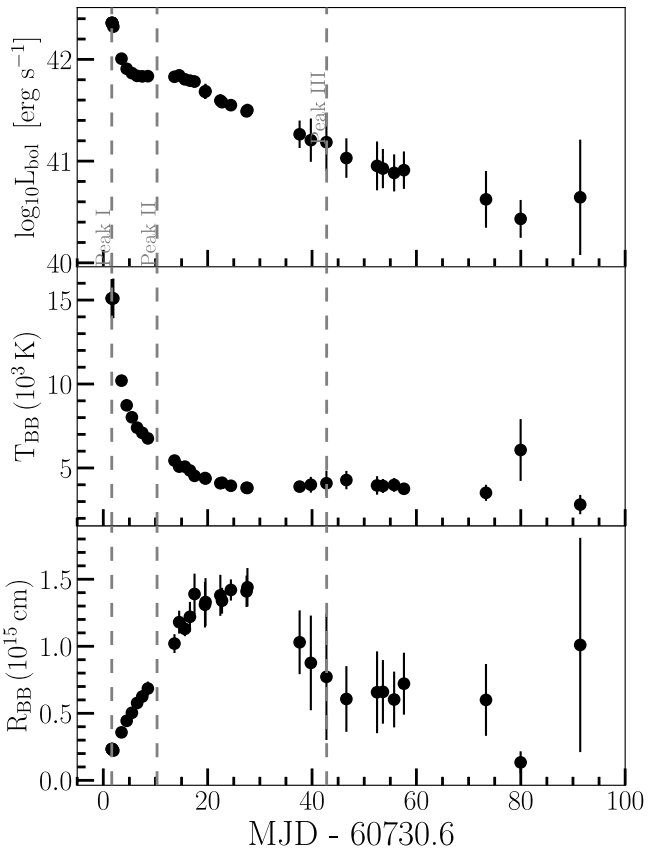

Figure 3. Top panel: bolometric light curve of SN 2025coe derived from fitting the multiband photometric results. Middle panel: temporal evolution of the blackbody temperature. Bottom panel: temporal evolution of the blackbody radius. The gray dashed lines mark the epochs of the multiple peaks detected from the multiband light curves. The bolometric light curve is available as the data behind the figure in the online journal.
(The data used to create this figure are available in the online article.)

2.2. Spectroscopy

Spectroscopic monitoring of SN 2025coe was conducted from $t = 0.9$ to $t = 87.4$ days. Table 2 shows a complete log of spectroscopy, which includes our observations conducted with Xinglong 2.16 m telescope (XL-216), Liverpool Telescope (LT), and Gran Telescopio Canarias (GTC), as well as publicly available spectra from Las Cumbres Observatory (LCO) network (T. M. Brown et al. 2013), retrieved from the Transient Name Server.

The data reduction for the spectra from XL-216 and LT follows the standard pipeline, including bias subtraction, flat-field correction, sky background removal, one-dimensional spectral extraction, wavelength calibration using comparison arcs, and flux calibration with standard stars. The raw data of the spectra from GTC were processed using the `PypeIt` pipeline (J. Prochaska et al. 2020). We applied photometry-based flux corrections to all the spectra to improve the flux calibration accuracy.

3. Analysis

3.1. Light-curve Properties

SN 2025coe was last nondetected in the ATLAS *o* band at MJD 60729.5. It was subsequently detected by ATLAS on MJD 60730.4. This constrains the explosion time of SN 2025coe to within 1 day. Shortly afterward, the astronomer Itagaki reported it at MJD 60730.6. We obtained the first multiband photometric data points for SN 2025coe at $t = 1.6$ days with TRT in the *BVRI* bands and at $t = 1.8$ day with Swift in the *uvw*2, *uvm*2, *uvw*1, *U*, *B*, and *V* bands. The first-epoch data across these bands indicate that SN 2025coe was very bright in the short-wavelength regimes at this early phase, suggesting the presence of a hot radiating source.

Following the initial observations, the *uvw*2, *uvm*2, *uvw*1, *U*, and *B* bands exhibit a fast decline in brightness, while the longer-wavelength bands continue to rise until $t \approx 10.2$ days, when the *R* band reaches its peak. Thereafter, the luminosity declines across all filters. However, at approximately $t \approx 42.8$ days, a possible third peak emerges in the *g*/*Gbp*/*G*/*Grp*/*I* bands, although this feature is not significant in other filters where the light-curve sampling is sparse. In this paper, we refer to the second peak (at $t \approx 10.2$ days) as the main peak.

3.1.1. Bolometric Light Curve

We derived the evolution of the bolometric luminosity $L_{\rm bol}$, blackbody temperature $T_{\rm BB}$, and radius $R_{\rm BB}$ with the `superbol` tool (M. Nicholl 2018). Figure 3 shows the

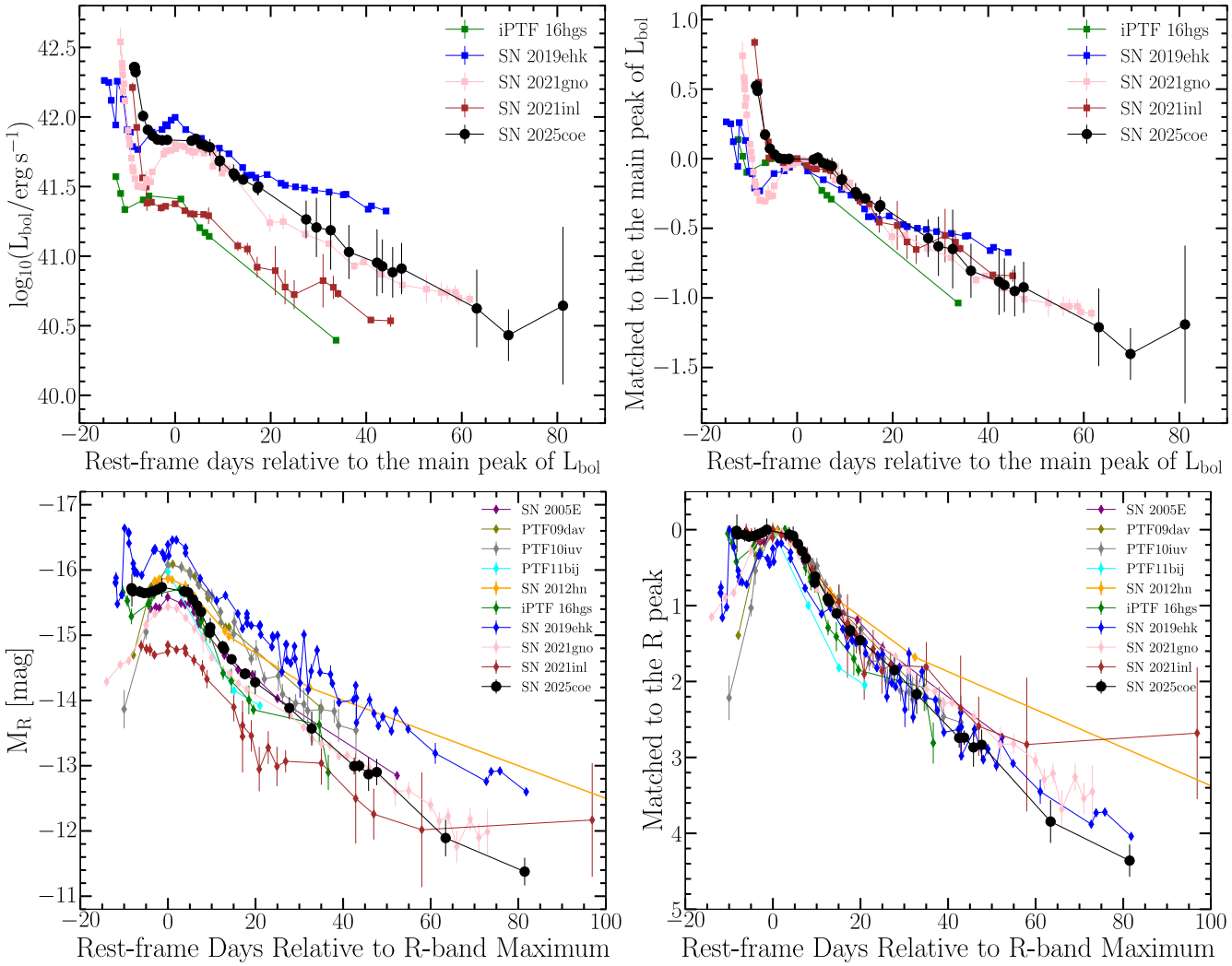

Figure 4. Top left: bolometric light curve of SN 2025coe (black dots) compared to other multipeaked CaSTs. Top right: scaled bolometric light curves (normalized to the main peak luminosity). Bottom left: *R*-band light curve of SN 2025coe (red dots) compared to other CaSTs (gray diamonds). Bottom right: scaled *R*-band light curves (normalized to the peak luminosity).

results, where we have marked the epochs of the multiple distinct peaks as mentioned in Section 3.1.

The first peak of the bolometric light curve reaches a luminosity of approximately 2.3×10^{42} erg s^{-1}, with a corresponding $T_{\rm BB} \simeq 15{,}000$ K and a $R_{\rm BB} \simeq 2.3 \times 10^{14}$ cm, indicating an initially very hot and luminous emitting region. After the first peak, the luminosity shows a rapid decline out to $t = 5$ days followed by a possible plateau near the main peak from $t = 5$ to 15 days. At the same time, $T_{\rm BB}$ cools down from 10,000 to 6000 K, while $R_{\rm BB}$ expands from 5.0×10^{14} to 1.1×10^{15} cm.

From $t = 15$ days, the luminosity decreases almost exponentially out to ~40 days. The possible third peak visible in the $g/Gbp/G/Grp/I$-band light curves cannot be clearly seen in the bolometric light curve. This is because the multiband monitoring of SN 2025coe has a very low cadence and covers only a limited number of filters during this late phase, resulting in large uncertainties in the derived bolometric luminosity at that epoch. Despite the large bolometric uncertainties, $T_{\rm BB}$ exhibits a slight increase at the third peak while $R_{\rm BB}$ remains nearly constant at $\sim 8.0 \times 10^{14}$ cm.

3.1.2. Comparison with Other CaSTs

We compare the bolometric and the *R*-band light curves of SN 2025coe with those of other CaSTs (H. B. Perets et al. 2010; M. M. Kasliwal et al. 2012; K. De et al. 2018; W. V. Jacobson-Galán et al. 2020, 2022; K. Ertini et al. 2023) in Figure 4. The bolometric luminosity of SN 2025coe is relatively high compared to other multipeaked CaSTs, while the main peak luminosity of SN 2025coe in the *R* band is typical compared to that of other CaSTs. By fitting the *R*-band light curve of SN 2025coe with a polynomial function, we determine that the peak luminosity of the main peak is $M_{R,\,\rm peak} \approx -15.8$ mag. The decline rates of both the bolometric and *R*-band light curves are typical among CaSTs.

3.2. Spectroscopic Properties

The spectroscopic evolution of SN 2025coe is presented in Figures 5 and 6. The first three spectra exhibit a featureless continuum from $t = 0.9$ to $t = 2.2$ days. There are no significant narrow emission lines from the flash ionization of the

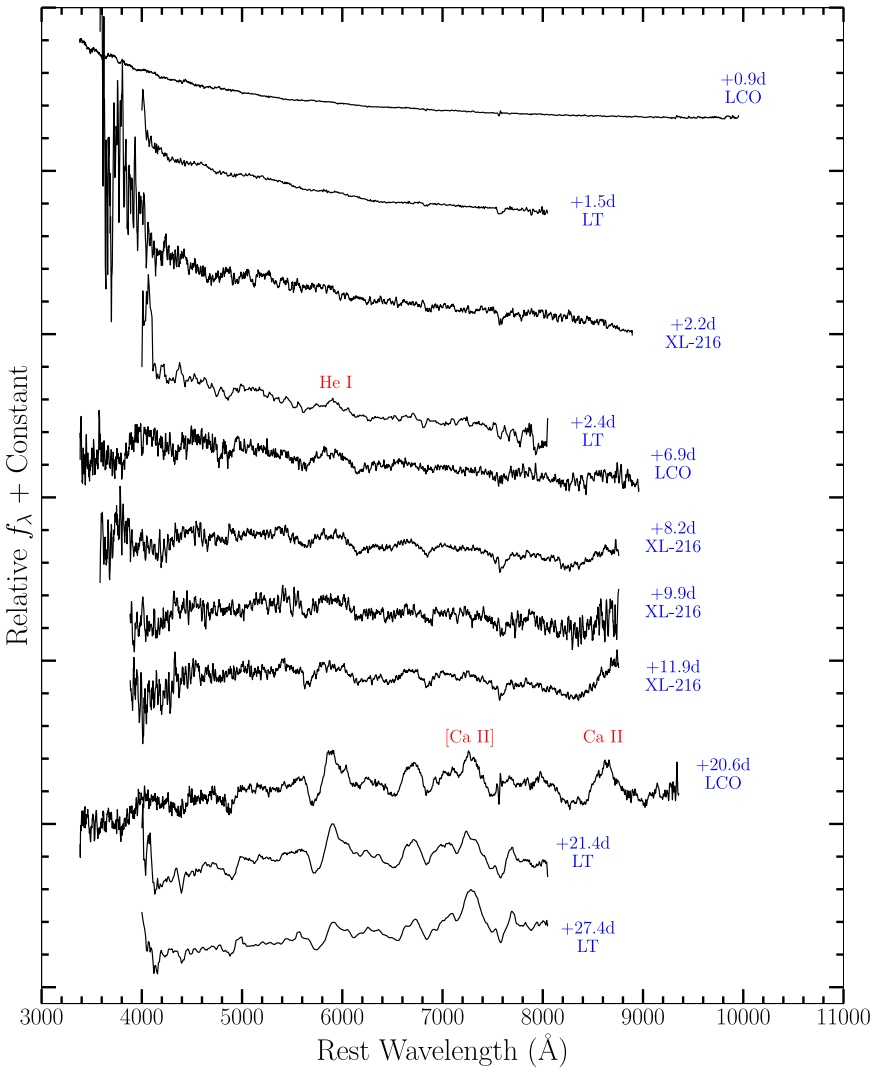

Figure 5. Spectroscopic evolution of SN 2025coe with phases (blue) marked with respect to the first detection in the clear band during the photospheric phase. The individual optical spectra are available as the data behind the figure in the online journal.
(The data used to create this figure are available in the online article.)

circumstellar medium (CSM) by the hot SN radiation or from ejecta–CSM interaction.

At $t = 2.4$ days, P Cygni profiles emerge in the spectrum, specially in the He I λ5876 line. These features persist until $t = 27.4$ days. We measure the absorption component of the He I λ5876 P Cygni profile using Gaussian profile fitting after removing the continuum baseline. The resulting line velocity $v_{\rm He\,I}$ is presented in Figure 7. It shows a rapid decrease from $\sim$ 22,000 km s^{-1} at $t = 2.4$ days to $\sim$6500 km s^{-1} by $t = 10$ days. Thereafter, $v_{\rm He\,I}$ remains nearly constant at $\sim$6500 km s^{-1} until $t = 27.4$ days.

At the time of $t = 20.6$ days, the forbidden emission line of calcium, [Ca II] $\lambda\lambda$7291, 7324, begins to emerge, when the ejecta are still optically thick given the P Cygni profiles of He I 5876. The P Cygni profile has disappeared at $t = 53.3$ days, signifying that the ejecta have transitioned to an optically thin state, marking the onset of the nebular phase in spectral evolution. During this phase, the spectrum exhibits strong [Ca II] lines and relatively weak [O I] $\lambda\lambda$6300, 6374 emission lines. These characteristics are fully consistent with the defining features of CaSTs: (1) rapid transition to the nebular phase ($\sim$a few $\times$ 10 days); (2) high flux ratio [Ca II]/[O I] during the nebular phase.

Figure 8 compares the [Ca II]/[O I] flux ratio of SN 2025coe with those of other CaSTs and SN subtypes. The [Ca II]/[O I] flux ratio of SN 2025coe exhibits an initial rise followed by a decline, resembling the behavior seen in another CaST, SN 2021gno (W. V. Jacobson-Galán et al. 2022). Moreover, at late phases, the [Ca II]/[O I] flux ratio of SN 2025coe declines rapidly, with a faster decay rate than any other CaSTs in the sample.

4. Modeling the Bolometric Light Curve

We first focus on interpreting the physical origin of the first peak. Previous studies have suggested that the rapid postpeak decline observed in CaSTs may originate from either (1) ejecta–CSM interaction (W. V. Jacobson-Galán et al. 2020) or (2) shock breakout followed by rapid cooling (K. De et al. 2018; W. V. Jacobson-Galán et al. 2020, 2022). The absence of detectable narrow emission lines in our early-phase spectra provides no evidence for the presence of CSM.

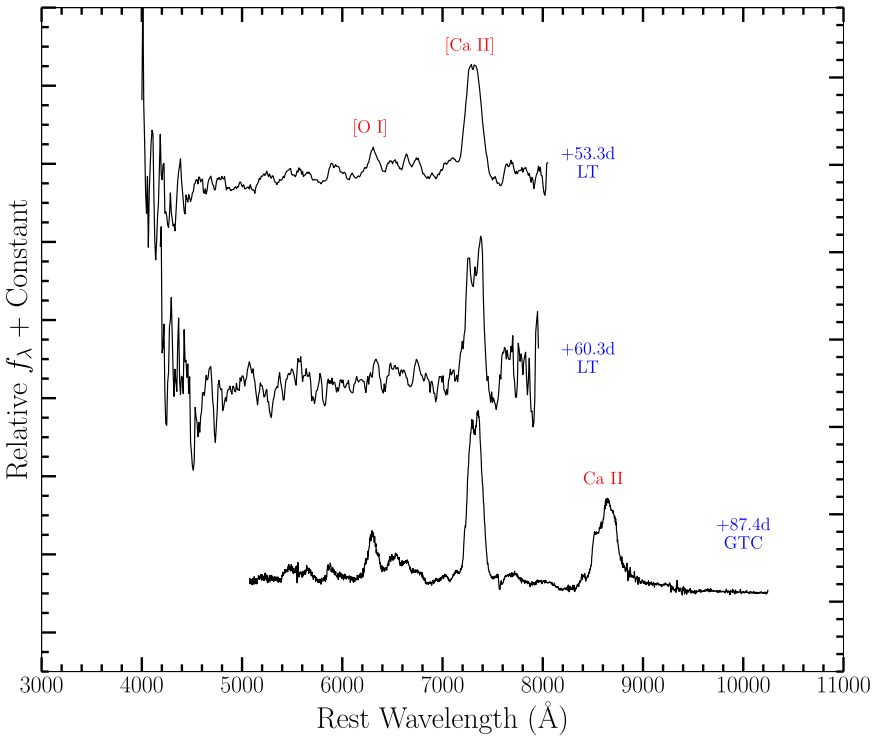

Figure 6. Spectroscopic evolution of SN 2025coe with phases (blue) marked with respect to the first detection in the clear band during the nebular phase. The individual optical spectra are available as the data behind the figure in the online journal.
(The data used to create this figure are available in the online article.)

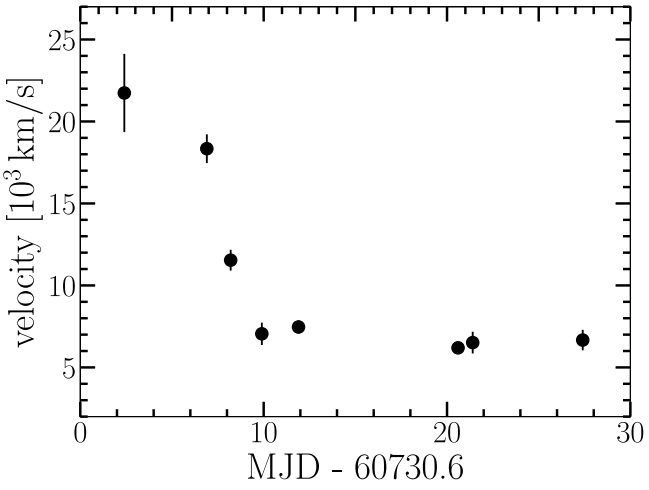

Figure 7. Line velocities $v_{\rm He\ I}$ obtained from He I λ5876 absorption profile fitting. The line velocities are available as the data behind the figure in the online journal.
(The data used to create this figure are available in the online article.)

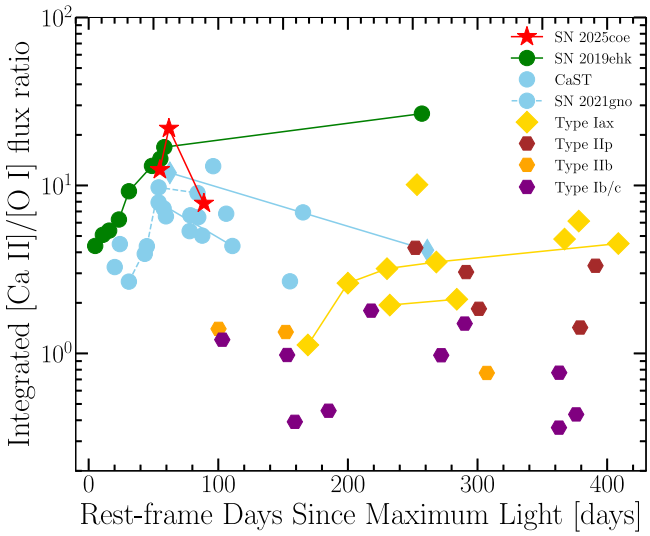

Figure 8. The [Ca II]/[O I] flux ratio of SN 2025coe in comparison with other CaSTs and different SN subtypes. The [Ca II]/[O I] flux ratio of SN 2025coe is available as the data behind the figure in the online journal.
(The data used to create this figure are available in the online article.)

In this work, we model the first bolometric light-curve peak using the shock cooling model. When the high-velocity ejecta collide with the extended material surrounding the progenitor, the resulting shock rapidly heats the impacted material. The shock-heated material exhibits high initial velocities, as measured from He I absorption line fitting (Figure 7). It then undergoes rapid adiabatic expansion and cooling, resulting in the observed steep decline in the early light curve. Here we adopt the shock cooling model described in A. L. Piro (2015) to quantitatively analyze the early photometric evolution (P. Venkatraman & W. Jacobson-Galán 2024).

Besides, we interpret the main peak of SN 2025coe as being powered by the radioactive decay of ^{56}Ni, consistent with other CaSTs, under the simplified assumption of the spherically symmetric ejecta. The light curve is analyzed separately for the early photospheric phase ($t < 30$ days) using the analytic solutions from Appendix A in S. Valenti et al. (2008; based on W. D. Arnett 1982) and for the nebular phase ($t > 60$ days) using the late-time solutions from the same reference (derived from P. G. Sutherland & J. C. Wheeler 1984; E. Cappellaro et al. 1997; S. A. Colgate et al. 1997).

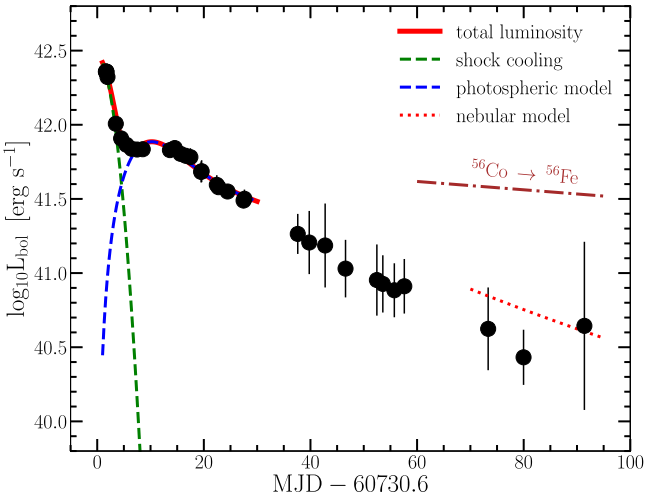

Figure 9. The bolometric light curve of SN 2025coe is shown together with the best-fit model of shock cooling + ^{56}Ni radioactive decay, where the dotted–dashed line represents the luminosity decline rate of the ^{56}Co radioactive decay.

Table 3
Summary of Best-fitting Parameters

Parameters	best-fit Value
R_e ($R_\odot$)	$13.5^{+64.1}_{-11.1}$
M_e ($10^{-3}\,M_\odot$)	$1.4^{+6.9}_{-1.2}$
v_s (10^4 km s^{-1})	$0.8^{+3.8}_{-0.6}$
E_k (10^{50} erg)	$1.7^{+4.2}_{-1.5}$
M_{ej} ($M_\odot$)	$0.29^{+0.14}_{-0.15}$
M_{Ni} ($10^{-2}\,M_\odot$)	$2.4^{+0.06}_{-0.05}$

Note. R_e: the radius of the extended material; M_e: the mass of the extended material; v_s: the shock velocity; E_k: the total kinetic energy of the ejecta, M_{Ni}: the synthesized ^{56}Ni mass; M_{ej}: the total ejecta mass.

We performed the combined model fitting to the bolometric light curve using the `emcee` Markov Chain Monte Carlo sampler (D. Foreman-Mackey et al. 2013). Here, we adopt a constant opacity of $\kappa_{sc} = 0.34\,cm^2\,g^{-1}$ for the shock cooling model (A. L. Piro 2015) and $\kappa_{rd} = 0.1\,cm^2\,g^{-1}$ in the radioactive decay model. The model constrains six physical parameters: the radius R_e and the mass M_e of the extended material, the shock velocity v_s, the total kinetic energy of the ejecta E_k, the synthesized ^{56}Ni mass (M_{Ni}), and the total ejecta mass (M_{ej}).

The best-fit results are presented in Figure 9 and Table 3. The results reveal an extended material configuration with a characteristic radius of $\sim$2.4–77.6 $R_\odot$ and a mass of ~ 0.2–$8.3 \times 10^{-3}\,M_\odot$. The results also indicate a total ejecta mass of $\sim 0.29\,M_\odot$ with ^{56}Ni mass of $\sim 0.02\,M_\odot$. The derived ^{56}Ni-to-ejecta mass ratio of $\sim$0.08 is consistent with the low ^{56}Ni fraction characteristic of the CaSTs population (H. B. Perets et al. 2010; A. W. Alsabti & P. Murdin 2017).

5. Discussion

In this work, we present extensive photometric and spectroscopic monitoring of the CaST SN 2025coe. Our observations reveal a triple-peaked light curve, and the first two peaks can be explained by a combination of shock cooling and radioactive heating. In this section, we discuss the progenitor properties of SN 2025coe and explore the physical origin of its possible third peak observed in multiband light curves.

Table 4
Summary of the Host Properties of Multipeaked CaSTs

Object Name	Host Galaxy	Host Type	Projected Offset
iPTF 16hgs[a]	SDSS J005052	…	6 kpc
SN 2018lqo[b]	CGCG 224-043	E	15.5 kpc
SN 2019ehk[c]	NGC 4231	SAB(s)bc	1.8 kpc
SN 2021gno[d]	NGC 4165	SAB(r)a	3.6 kpc
SN 2021inl[e]	NGC 4923	E/S0	23.3 kpc
SN 2025coe	NGC 3277	SAa/SAb	39.3 kpc

Notes. No systematic long-term photometric or spectroscopic follow-up observations are available for SN 2018lqo.
[a] K. De et al. (2018).
[b] K. De et al. (2020).
[c] W. V. Jacobson-Galán et al. (2020).
[d] W. V. Jacobson-Galán et al. (2022); K. Ertini et al. (2023).
[e] W. V. Jacobson-Galán et al. (2022).

5.1. Progenitor Properties

SN 2025coe's remote location from the host galaxy and the host's old stellar population promptly exclude massive star explosion models (A. W. Alsabti & P. Murdin 2017). Table 4 summarizes the host properties against other multipeak CaSTs. A plausible progenitor model is the double-WD merger model (A. Bobrick et al. 2017; H. B. Perets et al. 2019; Y. Zenati et al. 2019). Recent simulations show that the complete tidal disruption of a hybrid HeCO WD by a low-mass CO WD can trigger a weak He detonation on the primary, producing slightly lower mass of the ejecta ($\sim$0.01–0.1 $M_\odot$), and ^{56}Ni yields $\sim$a few $\times 10^{-4}$–$10^{-3}\,M_\odot$. Such values are broadly consistent with our model results shown in Table 3 (Y. Zenati et al. 2019).

During mass transfer from the secondary to the primary prior to the disruption, the transferred material forms an accretion disk due to its sufficiently large angular momentum. Y. Zenati et al. (2019) demonstrate that the inner region of the accretion disk may produce continuous outflow in the form of disk winds. The outflow expands outward to form CSM (C. Raskin & D. Kasen 2013). A fraction of the outflow might accumulate around the primary WD, forming a low-mass envelope (K. J. Shen et al. 2012; J. Schwab et al. 2016).

Our analysis of the bolometric luminosity of SN 2025coe reveals the presence of an extremely low-mass envelope surrounding its progenitor (see Table 3). The aforementioned double-WD merger model provides a natural explanation for the formation of such an envelope. Notably, this model has also successfully accounted for the observed properties of other multipeaked CaSTs (W. V. Jacobson-Galán et al. 2020, 2022).

5.2. The Potential Third Peak

We briefly examine the possible origin of the potential third peak detected in the multiband light curves of SN 2025coe. This feature is clearly visible in the $g/Gbp/G/Grp/I$ bands (see Figure 2), though our limited observational sampling in other wavelengths prevents further confirmation of its

presence. The temporal coincidence between this peak and a weak bump in the photospheric temperature evolution (see the middle panel in Figure 3) suggests a probably physical connection, likely involving the heating of the material.

A possible explanation involves interaction between the expanding ejecta and CSM or clump structures in the progenitor environment (W. V. Jacobson-Galán et al. 2020). The double-WD merger model naturally provides a physical origin for the formation of such CSM/clump structures through premerger mass loss and tidal disruption processes. Such ejecta–CSM/clump interaction naturally accounts for both the observed photospheric temperature increase and the emergence of the third luminosity peak. However, it is important to note that our spectroscopic sequence, presented in Figures 5 and 6, lacks spectroscopic coverage at around 42.8 days. Furthermore, the spectra at $t = 27.3$ and $t = 53.3$ days show no clear signs of ejecta–CSM/clump interaction. Therefore, this interpretation highlights the critical need for systematic, high-cadence, late-time monitoring of CaSTs, which would enable more robust characterization of their progenitor systems through detailed studies of CSM/clump properties and mass-loss histories.

The detection of similar features in future CaST observations could provide important insights into the diversity of progenitor channels and their mass-loss mechanisms. In particular, coordinated multiwavelength campaigns would help determine whether these third peaks (also detected in SN 2019ehk; W. V. Jacobson-Galán et al. 2020) represent a common phenomenon among CaSTs or are specific to certain progenitor configurations.

6. Conclusion

Our comprehensive study of SN 2025coe has revealed several remarkable properties that provide new insights into the nature of CaSTs. Through long-term photometric and spectroscopic observations, we have characterized this object as one of the members of its class. The key findings are summarized as follows:

1. SN 2025coe is located in the early-type galaxy NGC 3277 (morphological type SAa/SAb), with an exceptionally large projected physical offset of ~39.3 kpc (~317.″7) from the galactic center. This makes it the most distant multipeaked CaST ever discovered relative to its host galaxy, suggesting its progenitor system might be ejected through dynamical interactions (A. W. Alsabti & P. Murdin 2017).
2. Our multiband monitoring campaign, spanning from 1.6 to ~90 days relative to the first detection, reveals that SN 2025coe reached a peak absolute magnitude of $M_{R,\,\mathrm{peak}} \approx -15.8$ mag. The light curve exhibits a rapid postpeak decline rate of $\Delta m_{15}(R) \approx 1.5$ mag.
3. The well-sampled multiband light curves display multiple distinct peaks occurring at phases of approximately $t \approx 1.6$ and $t \approx 10.2$ days and a potential third peak at $t \approx 42.8$ days relative to the first detection. This triple-peaked structure is exceptionally rare among known CaSTs, with only one other event (SN 2019ehk) showing similar features.
4. Our spectroscopic sequence, beginning at just +0.9 day postdiscovery, shows (1) early-phase spectra dominated by broad (FWHM ~22,000 km s^{-1}) He I λ5876 emission; (2) the emergence of [Ca II] $\lambda\lambda$7291,7324 forbidden lines at $t = 20.6$ days while the spectrum still maintains photospheric characteristics of the He I P-Cygni profile; and (3) complete transition to the nebular phase by $t = 50.3$ days, marked by the disappearance of the He I P Cygni profile.
5. The nebular-phase spectrum of SN 2025coe shows a [Ca II]/[O I] flux ratio of >2.0, establishing SN 2025coe as a member of the CaST class. With its extensive photometric/spectroscopic sampling, it becomes the fifth confirmed case of CaSTs with at least two peaks, following iPTF 2018hgs, SN 2019ehk, SN 2021gno, and SN 2021inl. This growing sample enables statistical studies of their progenitor systems.
6. Our bolometric light-curve analysis using a combined shock cooling and ^{56}Ni-decay model yields best-fit parameters of $M_{\mathrm{ej}} \sim 0.29\,M_{\odot}$ for the ejecta mass and $M_{^{56}\mathrm{Ni}} \sim 0.02 M_{\odot}$. The modeling further reveals the presence of a low-mass envelope ($M_e \approx 2.0 \times 10^{-4}$–$8.3 \times 10^{-3}\,M_{\odot}$, $R_e \approx 2.4$–$77.6\,R_{\odot}$) surrounding the progenitor. The CO WD + hybrid WD disruption scenario naturally explains (1) the low ejecta and ^{56}Ni masses, (2) the origin of the envelope, and (3) the formation of extended CSM/clump. We propose that ejecta–CSM/clump interaction may be responsible for producing the observed third peak in the multiband light curves.

Future high-cadence transient surveys coupled with hydrodynamic simulations of such mergers will be crucial for testing whether this channel can account for the full diversity of observed CaST properties. In particular, well-sampled monitoring from ultraearly to late phases—as exemplified by facilities like The Mini-SiTian Array (Z.-J. Han et al. 2025), which can provide earlier detection and higher-cadence observations—will be essential. This must be complemented by real-time, multiband follow-up capable of dynamically increasing the cadence of photometric and spectroscopic observations in response to potential rebrightening or new peaks. Such a comprehensive approach is crucial for constraining the properties of the potential CSM/clump structures, thereby enabling a detailed reconstruction of the preexplosion circumstellar environments of CaSTs.

Acknowledgments

N.C.S. is funded by the Strategic Priority Research Program of the Chinese Academy of Sciences grant No. XDB0550300, the National Natural Science Foundation of China grants Nos. 12303051 and 12261141690, and the China Manned Space Program No. CMS-CSST-2025-A14. We acknowledge the support by the National Astronomical Research Institute of Thailand under project Nos. TRTToO_2025001 and TRTC12B_003. C.C. acknowledges the support of the China Scholarship Council (grant No. 202506380129). D.A. acknowledges financial support from the Spanish Ministry of Science and Innovation (MICINN) under the 2021 Ramón y Cajal program MICINN RYC2021-032609. F.P. acknowledges support from the Spanish Ministerio de Ciencia, Innovación y Universidades (MICINN) under grant No. PID2022-141915NB-C21. Z.G. acknowledges the support supported from the China-Chile Joint Research Fund (CCJRF No.2301) and the Chinese Academy of Sciences South America Center

for Astronomy (CASSACA) Key Research Project E52H540301. Z.G. is funded by ANID, Millennium Science Initiative, AIM23-001. W.X.L. is supported by NSFC (12120101003 and 12373010), the National Key R&D Program (2022YFA1602902 and 2023YFA1607804), and Strategic Priority Research Program of CAS (XDB0550100 and XDB0550000). L.Z.W. is sponsored by the National Natural Science Foundation of China (NSFC) grant No. 12573050, the Chinese Academy of Sciences South America Center for Astronomy (CASSACA) Key Research Project E52H540301, and in part by the Chinese Academy of Sciences (CAS) through a grant to the CASSACA. B.C.W. acknowledges support from the National Key R&D Program of China (grant Nos. 2023YFA1609700, 2023YFA1608304), the National Natural Science Foundation of China (NSFC; grant Nos. 12090040, 12090041, 12403022), and the Strategic Priority Research Program of the Chinese Academy of Sciences (grant Nos. XDB0550000, XDB0550100, XDB0550102). Z.X.N. acknowledges support from the NSFC through grant Nos. 12303039 and 12261141690. This work is part of the Project RYC2021-032991-I, funded by MICIU/AEI/10.13039/501100011033, and the European Union "NextGenerationEU"/PRTR.

We thank the staff at all participating observatories, including the Swift/UVOT facility, the Xinglong 2.16 m telescope, the Liverpool Telescope, the Thai Robotic Telescope network, and the Gran Telescopio Canaria, for their support during our observing campaigns.

We acknowledge the use of data and services provided by ATLAS, ZTF, and the Transient Name Server (TNS). We also acknowledge Moira Andrews and Joseph Farah for obtaining the LCO spectrum and making it publicly available via the TNS. We acknowledge the use of open-source software packages including astropy (Astropy Collaboration et al. 2013, 2018, 2022), AutoPhot (S. J. Brennan & M. Fraser 2022), emcee (D. Foreman-Mackey et al. 2013), IRAF (D. Tody 1986), and PypeIt (J. Prochaska et al. 2020).

ORCID iDs

Ning-Chen Sun https://orcid.org/0000-0002-4731-9698
Samaporn Tinyanont https://orcid.org/0000-0002-1481-4676
David Aguado https://orcid.org/0000-0001-5200-3973
Ismael Pérez-Fournon https://orcid.org/0000-0002-2807-6459
Frédérick Poidevin https://orcid.org/0000-0002-5391-5568
Justyn R. Maund https://orcid.org/0000-0003-0733-7215
Amit Kumar https://orcid.org/0000-0002-4870-9436
Junjie Jin https://orcid.org/0000-0002-8402-3722
Zhen Guo https://orcid.org/0000-0003-0292-4832
César Rojas-Bravo https://orcid.org/0000-0002-7559-315X
Rong-Feng Shen https://orcid.org/0000-0001-5012-2362
Lingzhi Wang https://orcid.org/0000-0002-1094-3817
Ziyang Wang https://orcid.org/0000-0002-0025-0179
Jie Zheng https://orcid.org/0000-0001-6637-6973
Alicia López-Oramas https://orcid.org/0000-0003-4603-1884
Zexi Niu https://orcid.org/0000-0002-3651-0681
Yanan Wang https://orcid.org/0000-0003-3207-5237
Klaas Wiersema https://orcid.org/0000-0002-9133-7957
Jifeng Liu https://orcid.org/0000-0002-2874-2706

References

Alsabti, A. W., & Murdin, P. 2017, Handbook of Supernovae (Springer)
Arnett, W. D. 1982, ApJ, 253, 785
Astropy Collaboration, Price-Whelan, A. M., Lim, P. L., et al. 2022, ApJ, 935, 167
Astropy Collaboration, Price-Whelan, A. M., Sipőcz, B. M., et al. 2018, AJ, 156, 123
Astropy Collaboration, Robitaille, T. P., Tollerud, E. J., et al. 2013, A&A, 558, A33
Bellm, E. C., Kulkarni, S. R., Graham, M. J., et al. 2019, PASP, 131, 018002
Bildsten, L., Shen, K. J., Weinberg, N. N., & Nelemans, G. 2007, ApJL, 662, L95
Bobrick, A., Davies, M. B., & Church, R. P. 2017, MNRAS, 467, 3556
Brennan, S. J., & Fraser, M. 2022, A&A, 667, A62
Brown, P. J., Breeveld, A. A., Holland, S., Kuin, P., & Pritchard, T. 2014, Ap&SS, 354, 89
Brown, T. M., Baliber, N., Bianco, F. B., et al. 2013, PASP, 125, 1031
Cappellaro, E., Mazzali, P. A., Benetti, S., et al. 1997, A&A, 328, 203
Colgate, S. A., Fryer, C. L., & Hand, K. P. 1997, ASIC, 486, 273
Darbha, S., Metzger, B. D., Quataert, E., et al. 2010, MNRAS, 409, 846
De, K., Fremling, U. C., Gal-Yam, A., et al. 2021, ApJL, 907, L18
De, K., Kasliwal, M. M., Cantwell, T., et al. 2018, ApJ, 866, 72
De, K., Kasliwal, M. M., Tzanidakis, A., et al. 2020, ApJ, 905, 58
Ertini, K., Folatelli, G., Martinez, L., et al. 2023, MNRAS, 526, 279
Filippenko, A. V., Chornock, R., Swift, B., et al. 2003, IAUC, 8159, 2
Fitzpatrick, E. L. 1999, PASP, 111, 63
Foley, R. J. 2015, MNRAS, 452, 2463
Foreman-Mackey, D., Hogg, D. W., Lang, D., & Goodman, J. 2013, PASP, 125, 306
Gehrels, N., Chincarini, G., Giommi, P., et al. 2004, ApJ, 611, 1005
Graham, M. J., Kulkarni, S. R., Bellm, E. C., et al. 2019, PASP, 131, 078001
Han, Z.-J., Li, Z.-Y., Chen, C., et al. 2025, RAA, 25, 044002
Henden, A. A., Welch, D. L., Terrell, D., & Levine, S. E. 2009, AAS Meeting, 214, 407.02
Itagaki, K. 2025, TNSTR, 756, 1
Jacobson-Galán, W. V., Margutti, R., Kilpatrick, C. D., et al. 2020, ApJ, 898, 166
Jacobson-Galán, W. V., Venkatraman, P., Margutti, R., et al. 2022, ApJ, 932, 58
Kasliwal, M. M., Kulkarni, S. R., Gal-Yam, A., et al. 2012, ApJ, 755, 161
Lunnan, R., Kasliwal, M. M., Cao, Y., et al. 2017, ApJ, 836, 60
Lupton, R., & Ivezić, Ž. 2005, ASPC, 338, 151
Lyman, J. D., Levan, A. J., Church, R. P., Davies, M. B., & Tanvir, N. R. 2014, MNRAS, 444, 2157
Mould, J. R., Huchra, J. P., Freedman, W. L., et al. 2000, ApJ, 529, 786
Mulchaey, J. S., Kasliwal, M. M., & Kollmeier, J. A. 2014, ApJL, 780, L34
Nakaoka, T., Maeda, K., Yamanaka, M., et al. 2021, ApJ, 912, 30
Nicholl, M. 2018, RNAAS, 2, 230
Perets, H. B., Gal-Yam, A., Mazzali, P. A., et al. 2010, Natur, 465, 322
Perets, H. B., Zenati, Y., Toonen, S., & Bobrick, A. 2019, arXiv:1910.07532
Piro, A. L. 2015, ApJL, 808, L51
Polin, A., Nugent, P., & Kasen, D. 2021, ApJ, 906, 65
Prochaska, J., Hennawi, J., Westfall, K., et al. 2020, JOSS, 5, 2308
Raskin, C., & Kasen, D. 2013, ApJ, 772, 1
Roming, P. W. A., Kennedy, T. E., Mason, K. O., et al. 2005, SSRv, 120, 95
Scherbak, P., Polin, A., Kasliwal, M., et al. 2025, PASP, 137, 114207
Schlafly, E. F., & Finkbeiner, D. P. 2011, ApJ, 737, 103
Schwab, J., Quataert, E., & Kasen, D. 2016, MNRAS, 463, 3461
Sell, P. H., Maccarone, T. J., Kotak, R., Knigge, C., & Sand, D. J. 2015, MNRAS, 450, 4198
Shen, K. J., Bildsten, L., Kasen, D., & Quataert, E. 2012, ApJ, 748, 35
Shen, K. J., Kasen, D., Weinberg, N. N., Bildsten, L., & Scannapieco, E. 2010, ApJ, 715, 767
Shen, K. J., Quataert, E., & Pakmor, R. 2019, ApJ, 887, 180
Sim, S. A., Fink, M., Kromer, M., et al. 2012, MNRAS, 420, 3003
Sutherland, P. G., & Wheeler, J. C. 1984, ApJ, 280, 282
Thuillot, W., Midavaine, T., Dennefeld, M., Buil, C., & Neveu, S. 2022, in SF2A-2022: Proc. Annual Meeting of the French Society of Astronomy and Astrophysics, ed. J. Richard et al., 149
Tody, D. 1986, SPIE, 627, 733
Tonry, J. L., Denneau, L., Flewelling, H., et al. 2018a, ApJ, 867, 105
Tonry, J. L., Denneau, L., Heinze, A. N., et al. 2018b, PASP, 130, 064505
Valenti, S., Benetti, S., Cappellaro, E., et al. 2008, MNRAS, 383, 1485
Venkatraman, P., & Jacobson-Galán, W. 2024, RNAAS, 8, 33
Waldman, R., Sauer, D., Livne, E., et al. 2011, ApJ, 738, 21
Woosley, S. E., & Kasen, D. 2011, ApJ, 734, 38
Yuan, F., Kobayashi, C., Schmidt, B. P., et al. 2013, MNRAS, 432, 1680
Zenati, Y., Perets, H. B., & Toonen, S. 2019, MNRAS, 486, 1805